

# Vertical Heterogeneous Integration of Metal Halide Perovskite Quantum-Wires/Nanowires for Flexible Narrowband Photodetectors

Daquan Zhang, Yudong Zhu, Qianpeng Zhang, Beita Ren, Bryan Cao, Qizhen Li, Swapnadeep Poddar, Yu Zhou, Xiao Qiu, Zhuhong He, and Zhiyong Fan\*



Cite This: <https://doi.org/10.1021/acs.nanolett.2c00383>



Read Online

ACCESS |



Metrics & More



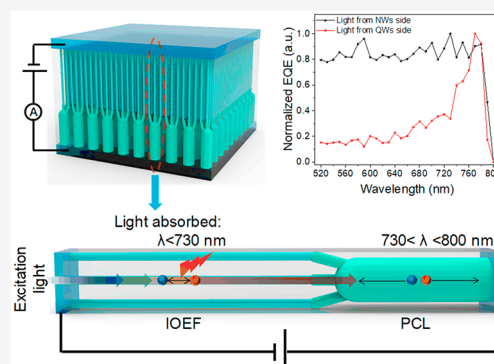
Article Recommendations



Supporting Information

**ABSTRACT:** Charge collection narrowing (CCN) has been reported to be an efficient strategy to achieve optical filter-free narrowband photodetection (NPD) with metal halide perovskite (MHP) single crystals. However, the necessity of utilizing thick crystals in CCN limits their applications in large scale, flexible, self-driven, and high-performance optoelectronics. Here, for the first time, we fabricate vertically integrated MHP quantum wire/nanowire (QW/NW) array based photodetectors in nanoengineered porous alumina membranes (PAMs) showing self-driven broadband photodetection (BPD) and NPD capability simultaneously. Two cutoff detection edges of the NPDs are located at around 770 and 730 nm, with a full-width at half-maxima (fwhm) of around 40 nm. The optical bandgap difference between the NWs and the QWs, in conjunction with the high carrier recombination rate in QWs, contributes to the intriguing NPD performance. Thanks to the excellent mechanical flexibility of the PAMs, a flexible NPD is demonstrated with respectable performance. Our work here opens a new pathway to design and engineer a nanostructured MHP for novel color selective and full color sensing devices.

**KEYWORDS:** metal halide perovskites, nanowires, quantum wires, porous alumina membranes, flexible narrowband photodetectors



Benefiting from the excellent optoelectronic properties, such as high light extinction coefficient, long carrier diffusion length, and high mobility, to name but a few, metal halide perovskite (MHP) broadband photodetection (BPD) devices have been fabricated with ultrahigh responsivity, detectivity, and sensitivity in both single crystalline and polycrystalline films.<sup>1–5</sup> The broad detection range can encompass the whole spectrum from X-ray to the near-infrared light, making it propitious in gray scale imaging,<sup>6</sup> biological sensing,<sup>7</sup> and communication applications.<sup>8</sup> Meanwhile, thanks to the low temperature fabrication process, the flexible MHP BPD device has also been extensively explored, revealing its great potential in the future wearable optoelectronics.<sup>9,10</sup> To further achieve the color discrimination and improve the sensing/communication precision and resolution, narrowband photodetections (NPDs) have also been demonstrated with MHP materials recently via the carrier collection narrowing (CCN) effect.<sup>11–16</sup> Different from the conventional techniques (color filters,<sup>17,18</sup> narrow absorption absorbers,<sup>19</sup> and plasmonic effect<sup>20</sup>) for NPDs, CCN is realized using the difference on penetration depth for different optical wavelengths, in conjunction with strong surface-charge recombination of short wavelength light-generated carriers induced by the surface states. These two mechanisms lead to NPD of near band-edge optical wavelength, which thus significantly reduces the device complexity and fabrication cost. However, thick crystals (>20

μm) are usually needed to achieve a strong CCN effect, which obviously limits their applications in flexible optoelectronics. In addition, one single device operating in both BPD and NPD modes is also attractive for real applications;<sup>13,16</sup> however, most of the current reports on this topic only demonstrate a single NPD mode.

To our best knowledge, all of the reported MHP NPDs have used planar/bulk material on rigid substrates. Even though MHP nanowires (NWs) have shown significant advantages over their thin film or bulk counterparts in photodetectors and image sensors, owing to their unique one-dimensional morphology and carrier transportation properties,<sup>21–30</sup> MHP NW based NPDs have not been demonstrated so far. There are two possible reasons: (1) the lack of mature techniques to grow long enough vertically aligned MHP NW arrays to leverage light penetration depth and separate different wavelengths and (2) efficient carrier transportation capability in MHP NWs thwarting the CCN effect. In view of these bottleneck challenges, innovations on both MHP NW growth

**Received:** January 28, 2022

**Revised:** March 11, 2022

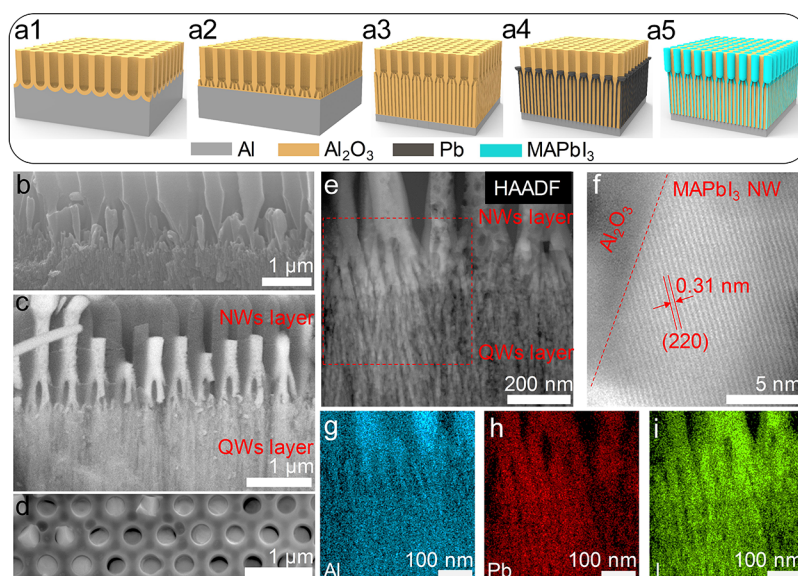


**Figure 1.** MAPbI<sub>3</sub> QW/NW array fabrication and characterization. a, Schematic of the fabrication process: a1, 200 V anodization; a2, barrier thinning; a3, 5 V anodization; a4, Pb electrochemical deposition; a5, VSSR growth. b and c, Cross-sectional SEM images of a PAM without (b) and with (c) MAPbI<sub>3</sub> QWs/NWs growth. The image (c) was taken in BSE measurement mode. d, A top view SEM image of MAPbI<sub>3</sub> QWs/NWs embedded in the perfectly ordered PAM. e and f, HAADF-STEM images of the MAPbI<sub>3</sub> QW/NW junction under low (e) and high (f) magnification. g–i, Selective area (red dash line marked in e) EDX mapping of the MAPbI<sub>3</sub> QW/NW junction.

and device structural design are in urgent need to realize MHP NW NPD.

In this work, we demonstrate a vertically and heterogeneously integrated MAPbI<sub>3</sub> quantum wire/NW (QW/NW) arrays in porous alumina membranes (PAMs) sandwiched by two transparent electrodes for photodetectors exhibiting both BPD and NPD functions when light is shone at different sides. In this unique architecture, an ultrahigh-density small diameter ( $\sim 6$  nm) MAPbI<sub>3</sub> QW array with a thickness of  $\sim 2.3$   $\mu\text{m}$  is located on top of an array of large diameter ( $\sim 200$  nm) MAPbI<sub>3</sub> NWs. The QW and NW layers work as the internal optoelectronic filter (IOEF) and photoconversion layer (PCL), separately. Although QWs and NWs are made of the same material, quantum confinement leads to a widened optical bandgap and increased radiative recombination in QWs. The bandgap difference between the NWs and QWs, in conjunction with the high carrier recombination rate in QWs,<sup>31</sup> contributes to the NPD characteristic when the light is shone from the QW side. Two cutoff detection edges of the NPDs are located at around 770 and 730 nm. The full-width at half-maxima (fwhm) of the NPD (external quantum efficiency) EQE spectrum is  $\sim 40$  nm, and the maximum EQE is 1.71% under  $-0.5$  V bias. The device can also operate under zero bias, showing the potency for self-driven optoelectronics. Meanwhile, benefiting from the excellent mechanical flexibility of PAM templates,<sup>32,33</sup> flexible NPDs are also demonstrated with good performance. To the best of our knowledge, this is the first demonstration of filterless flexible NPDs utilizing MHP NWs. Our findings open a new vista of designing and engineering nanostructured MHP to build a new class of color selective and full color photodetectors.

The QW/NW array growth process is schematically shown in Figure 1a. It primarily comprises two steps: dual-diameter PAM fabrication (Figure 1a1–a3) and vapor–solid–solid reaction (VSSR) assisted MAPbI<sub>3</sub> growth (Figure 1a4,a5). Since the PAM pore size is proportional to the anodization voltage, the dual-diameter PAM is fabricated via a two-step

electrochemical anodization of aluminum (Al) foil with different voltages. Specifically, a high voltage (200 V) anodization is first carried out to obtain large pore PAM (Figure 1a1), whose average pore size of  $\sim 200$  nm can be observed from the corresponding scanning electron microscopy (SEM) image (Figure 1b). Subsequently, an extra barrier thinning process (Figure 1a2) is conducted to render the barrier layer (Al<sub>2</sub>O<sub>3</sub>) thin enough for the succeeding low voltage anodization. As shown in Figure 1b, this barrier thinning process produces many fine channels in the barrier layer, which enables the electrical contact between the bottom Al and the anodization electrolyte. The transition zone, so-called subchannels, has a tapering shape with diameters decreasing gradually from  $\sim 200$  nm to  $<10$  nm. Finally, a 5 V anodization is executed to obtain ultrasmall pores (Figure 1a3). The SEM image in Figure 1b clearly shows the unique dual diameter structure with large pores at the top and the underlying ultrahigh-density small pores. Thereafter, Pb metal electrodeposition (Figure 1a4) and VSSR (Figure 1a5) are successively carried out for the MAPbI<sub>3</sub> NW growth. To make sure the Pb precursor amount is enough for MAPbI<sub>3</sub> NW growth, a mixture of aqueous and nonaqueous solvent is used as the electrolyte for Pb electrodeposition to avoid water splitting (details in Methods). The VSSR process was performed using the same growth setup and conditions that we have reported before.<sup>21,31</sup> Note that this unique fabrication process can be uniformly scaled up to even a 4-in. wafer scale,<sup>34</sup> which is one of the advantages over the MHP single crystal based NPD device fabrication. The QW/NW arrays can be easily distinguished by the brightness contrast in the cross-sectional back-scattered electron (BSE) SEM image (Figure 1c), where the dark area is anodic alumina and the light area represents MAPbI<sub>3</sub>, with the energy-dispersive X-ray (EDX) results shown in Figure S1. Figure 1d and Figure S1f show the top-view SEM images of MAPbI<sub>3</sub> NWs in perfectly ordered and semiordered PAMs, respectively. Note that such a perfectly ordered PAM is fabricated by the nanoimprint

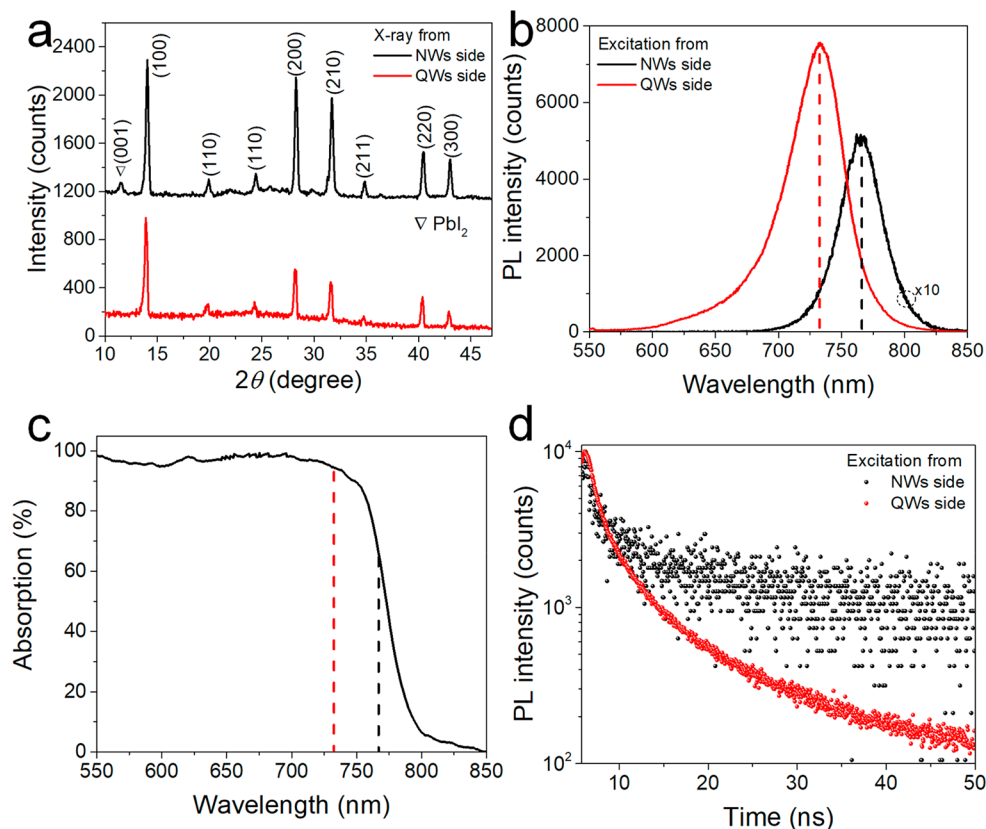


**Figure 2.** MAPbI<sub>3</sub> QWs/NWs characterization. a, XRD patterns with the X-ray separately shining from the NW and QW sides. b, PL spectra with excitation light ( $\lambda_{\text{ex}} = 350$  nm) separately shining from the NW and QW sides. c, UV-vis absorption spectrum of the MAPbI<sub>3</sub> QW/NW arrays. d, TRPL ( $\lambda_{\text{ex}} = 365$  nm) measured at the PL peaks for MAPbI<sub>3</sub> NWs and QWs with excitation from the NW and QW sides, separately.

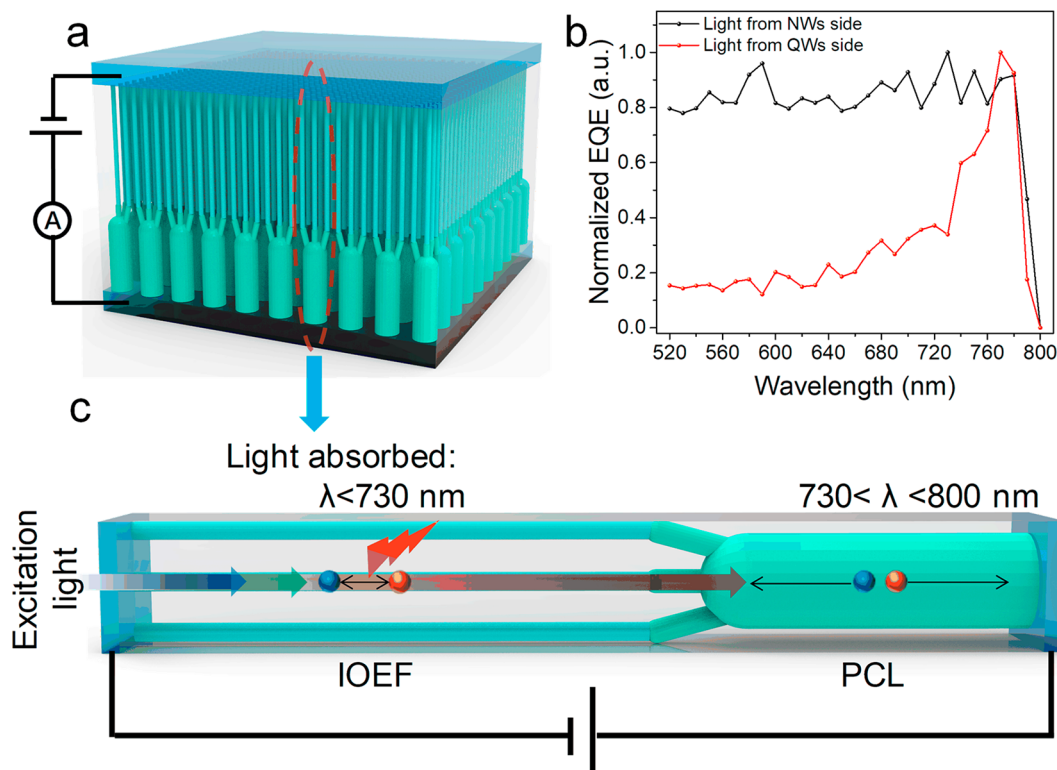


**Figure 3.** NPD device operation mechanism. a, Schematic of the device with ITO electrodes at both sides of the QW/NW arrays. b, Wavelength dependent normalized EQE spectra with light from both the NW and the QW sides. c, Schematic of an enlarged QW/NW junction under light and bias conditions.

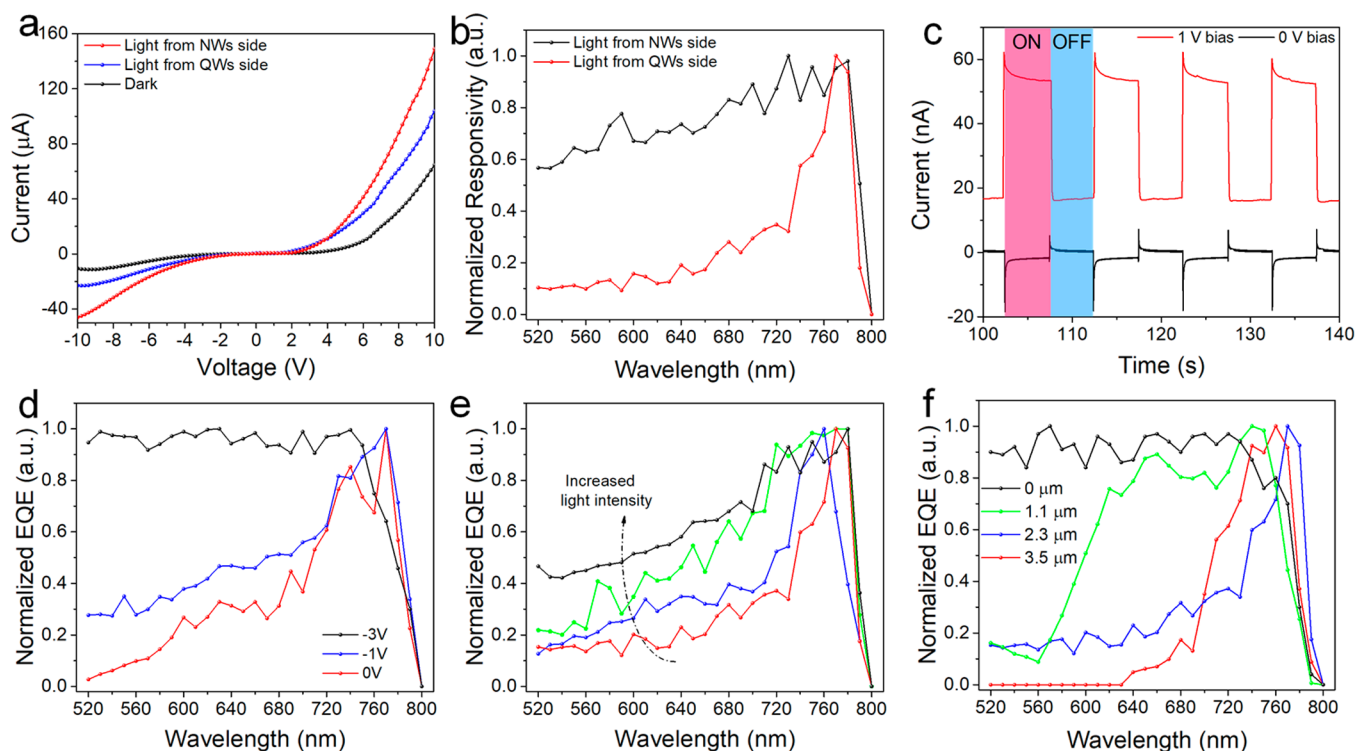


**Figure 4.** NPD performance characterization. a,  $I$ – $V$  curves under dark and white light ( $10 \text{ mW cm}^{-2}$ ) conditions. b, Normalized responsivity spectra with light shining from both the NW and the QW sides. c, Time domain current change with repeated white light ( $10 \text{ mW cm}^{-2}$ ) ON and OFF. The applied voltages are 0 and 1 V, respectively. d–f, Normalized EQE spectra under different operation conditions: d, bias voltages; e, light intensities, and f, QW layer thicknesses.

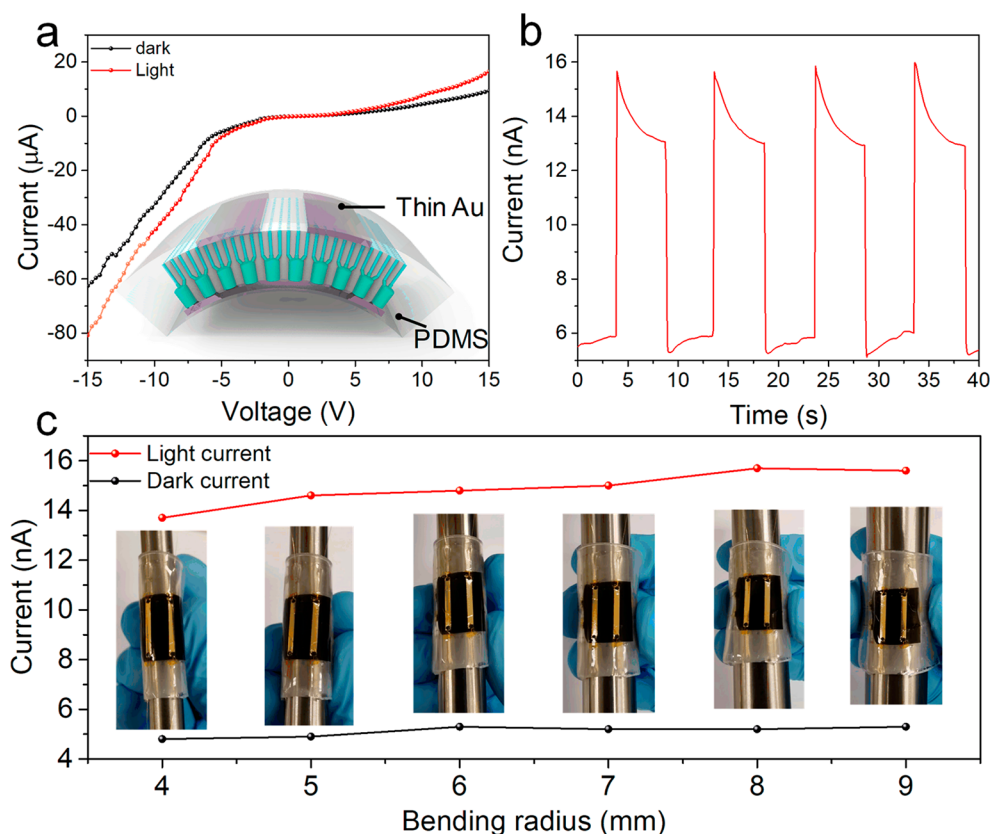
method in conjunction with the anodization process, which is useful for addressing the individual NWs in ultrahigh resolution imaging applications.

Figure 1e shows a low magnification high angle angular dark field–scanning transmission electron microscopy (HAADF-STEM) image of the QW/NW transition area where the ultrahigh-density QWs can be easily seen. The high magnification image in Figure 1f shows the boundary between  $\text{Al}_2\text{O}_3$  and  $\text{MAPbI}_3$  NWs, where both the good crystallinity and surface passivation can be seen. It is mainly attributed to the high temperature VSSR growth in the  $\text{Al}_2\text{O}_3$  template.<sup>21,31</sup> Figure 1g–i shows EDX mapping of the marked area in Figure 1e. The uniform element distribution in both NWs and QWs demonstrates excellent material quality as well.

Figure 2a shows the X-ray diffraction (XRD) patterns of the  $\text{MAPbI}_3$  QW/NW arrays with light shining from NWs and QWs separately, where only one set of crystalline peaks can be seen, which indicates the same cubic crystal structure for both NWs and QWs. Note that, in order to shine an X-ray from the QW side, the entire QW/NW structure is delaminated from the Al substrate (Methods). A small XRD peak at around  $11.5^\circ$  for the NWs can be attributed to the  $\text{PbI}_2$  (001) phase, as labeled in Figure 2a. It is invisible for QWs because the perovskite decomposition process always starts from the top surface of the NWs. Figure 2b shows the photoluminescence (PL) spectra of QWs and NWs when the excitation light is shone from each side. It can be seen that two PL peaks are located at 731 and 766 nm, corresponding to the optical bandgap values of 1.70 and 1.61 eV for  $\text{MAPbI}_3$  QWs and NWs, respectively. The obvious PL signal enhancement for QWs, as well as the bandgap increase, is induced by the quantum confinement and surface passivation, which have

been systematically studied in our previous report.<sup>31</sup> The PL spectra of the perovskite NWs in the subchannels are shown in Figure S2, demonstrating a similar peak position and intensity as those of main-channel NWs. Figure 2c shows the UV–vis absorption spectrum of the QW/NW arrays, where two absorption edges ( $\sim 770 \text{ nm}$  and  $\sim 730 \text{ nm}$ ) can be seen and are attributed to the NWs and QWs, respectively. The time-resolved PL (TRPL) curves in Figure 2d and the double-exponential fitting results in Table S1 show the average carrier lifetimes of 3.04 and 2.40 ns for the NWs and QWs, respectively. Usually, a short carrier lifetime means short carrier diffusion length and high defect concentration, leading to more nonradiative recombination. However, we have previously reported that the short diffusion length in perovskite QWs is mainly caused by quantum confinement induced strong radiative recombination, which NWs lack.<sup>31</sup> The severe carrier recombination loss in QWs makes it promising in working as the IOEF.

The QW/NW heterogeneous array based photodetector structure is schematically demonstrated in Figure 3a. The QW layer thickness is controlled and tuned by the 5 V anodization time. After etching away the Al substrate, the 150 nm ITO electrode is sputtered onto both sides with low radio frequency (RF) power (50 W) to minimize the damage to the perovskites. Figure 3b shows the normalized EQE spectra of the device with different light excitation directions. It is intriguing that the device shows broadband response capability when the light is from the NW side, while it operates as a NPD device when the light is shone from the other side. Two cut off edges of the NPD EQE spectrum are located at around 770 and 730 nm, matching with the light absorption/PL peak positions of NWs and QWs, respectively. The fwhm is



**Figure 5.** Flexible NPD demonstration. a,  $I$ - $V$  curves of a bent device (bending radius 9 mm) under dark and light conditions. The inset shows a schematic of a flexible device. b, Time domain current change of a bent device (bending radius 9 mm) with the light repeatedly ON and OFF. Bias voltage is 0.5 V. c, Bending radius dependent dark and light current change of a flexible device. Bias voltage is 0.5 V. The light was shined at the QW side for all the measurements.

positioned at around 40 nm, which is much smaller than that of some reported MHP NPDs (Table S2).

Different from the surface trap state in previous reported NPDs, we propose the mechanism of our QW/NW array based NPDs to be the carrier recombination loss dominated in the QW layer. The QW layer has a larger bandgap and much higher carrier recombination rate, working as the IOEF, while the NW layer has very good carrier transportation capability, working as the PCL. As illustrated in Figure 3c, when the light is shone from the QWs side, short wavelength ( $<730$  nm) light will be absorbed and electron-hole pairs (EHPs) will be generated within the QWs. These EHPs are too far to be collected by the counter electrode, and the majority of them will be lost via strong radiative recombination in QWs. Therefore, such recombination loss suppresses the responsivity to short wavelength light. However, for those photons with energy values between the bandgap of QWs and NWs, they can mostly penetrate through the QWs and subsequently be absorbed by the NWs. Considering the good carrier transportation along the NWs, those photogenerated carriers can be readily collected by the nearby ITO electrode and contribute to the output photocurrent. Consequently, CCN is realized with such a unique QW/NW heterogeneous structure. Note that the total device thickness is only  $3.5 \mu\text{m}$ , which is significantly thinner than previously reported NPD devices, making it promising in flexible optoelectronics.<sup>21</sup> In comparison, when the light is shone from the NW side, the majority of the light, especially the shorter wavelength portion, will be immediately absorbed within the NWs following the Beer-

Lambert law. All of those photogenerated carriers contribute to the photocurrent, and hence it operates as a BPD device. The absolute EQE spectra of the device working at the BPD and NPD modes are shown in Figure S4.

The current-voltage ( $I$ - $V$ ) curves are measured under dark and white light ( $10 \text{ mW cm}^{-2}$ ) conditions, as shown in Figure 4a. The diode behavior mainly stems from the barrier layer induced metal-insulator-semiconductor (MIS) junction, with the threshold voltage being  $\sim 5$  V. The detailed band alignment is shown in Figure S5. The normalized responsivity spectra are presented in Figure 4b, confirming the NPD capability of the device. The time domain-current ( $I$ - $t$ ) curves are shown in Figure 4c, from which stable photodetection performance can be seen. The overshoot of the photocurrent under bias voltage is mainly ascribed to the ion migration in perovskite NWs.<sup>35</sup> However, under 0 V bias, the ion migration is negligible, and the shift/realignment of the quasi-Fermi levels will induce an obvious overshoot at both light ON and OFF moments.<sup>36</sup> It is applicable for various semiconductors adjacent to the junction/interface in response to the excitation and thermal effect of the illumination light under nonequilibrium conditions. The response (rise/fall) time are extracted to be 81/165 ms and 13/6.7 ms for 1 and 0 V bias, respectively (Figure S6). More NPD performances are characterized under different bias voltages, light intensities, and device thicknesses, as shown in Figure 4d-f. We first explore the dependence of the NPD performance on the operation bias (Figure 4d). It can be seen that the EQE curve at zero bias shows a narrow response peak, indicating its potential in self-driven optoelectronics. The EQE

value increases gradually in the short wavelength range with increased bias. This is caused by the increased electric field induced longer carrier drift distance and hence higher carrier collection efficiency in QWs. In particular, when the absolute bias voltage is higher than 3 V, the narrowband response behavior is gone, at which condition the electric field dominated drift separates all those photogenerated carriers and transports them to the ITO electrode, regardless of the strong radiative recombination in QWs. The light intensity dependent photoresponse is measured and shown in Figure 4e, with the light intensities shown in Figure S7. The bias voltage is kept constant at  $-0.5$  V. It can be seen that the EQE value at short wavelength gradually increases with increased light intensity. We also tune the QW layer thickness with cross-sectional SEM images shown in Figure S8 and study the NPD performance under a consistent bias voltage of  $-0.5$  V. It can be seen that, when decreasing the QW layer thickness, the EQE at shorter wavelength is gradually increased, which means that the CCN effect is fading away. When the QW layer is as thin as  $1.1 \mu\text{m}$ , the whole device almost becomes a BPD device. We attribute this result to the nonefficient light absorption in the thinner QW layer, as well as the increased electric field inside. Considering that the light absorption follows the Beer–Lambert law, shorter wavelength light can penetrate into the NW layer when reducing the QW layer. Those light generated carriers can then be collected by the electrode easily. Meanwhile, it is noted that the longer 5 V anodization process causes delamination of the large-channel layer, resulting in the maximum achievable QW layer of only around  $3.5 \mu\text{m}$ .

Finally, utilizing the excellent mechanical flexibility of PAMs (Figure S9), a flexible NPD is demonstrated by replacing the rigid ITO electrode with a thin ( $50 \text{ nm}$ ) Au electrode. The  $I$ – $V$  and  $I$ – $t$  curves of a bended device (bending curvature:  $9 \text{ mm}$ ) under dark and white light ( $10 \text{ mW cm}^{-2}$ ) conditions are shown in Figure 5a,b, separately. It can be seen that the bended device still shows certain photodetection performance, which can be further improved by utilizing other transparent flexible electrodes, such as Ag NWs,<sup>37</sup> and inkjet printed inorganic conductive materials.<sup>38,39</sup> Different bending radii with an effective area of  $1.5 \text{ cm} \times 1.5 \text{ cm}$  are further explored and shown in Figure 5c, where no obvious change in the light and dark current is observed under different bending conditions.

In summary, a vertical heterogeneously integrated MHP QW/NW NPD device structure has been successfully fabricated using a dual-diameter PAM template assisted VSSR process. The QW/NW array based photodetectors can operate under both BPD and NPD modes when the light is shone from two different sides. The NPD behavior is mainly ascribed to the optical bandgap difference between NWs and QWs, in conjunction with high carrier recombination rate in QWs. Owing to the excellent mechanical flexibility of the PAMs, a flexible NPD is demonstrated with good bendability. Overall, the unique architecture presented in this work provides a promising approach to realize filter-free, spectrum tunable, and flexible NPDs. In principle, if Br and Cl halide perovskites, or mixed halide perovskites, are used as the base material, NPDs with a selective response to green and blue color light can be obtained. With a proper integration method, full color photodetection can potentially be achieved. This can find a broad spectrum of optoelectronic applications in the future.

## METHODS

**Materials.** All the chemicals were purchased from Sigma-Aldrich and used as received without further purification.

**Dual-Diameter PAM Template Fabrication.** The dual-diameter PAMs were fabricated via a two-step anodic anodization process. First, pure Al foil with a thickness of  $0.25 \text{ mm}$  was cut into  $1.5 \text{ cm} \times 2.5 \text{ cm}$  pieces and cleaned with acetone, isopropyl alcohol, and deionized (DI) water successively. The chip was then electrochemically polished in a mixture solution of  $\text{HClO}_4$  and  $\text{CH}_3\text{CH}_2\text{OH}$  (1:3 in vol) for  $2.5 \text{ min}$  under  $12.5 \text{ V}$  and room temperature conditions. To get the perfectly ordered nanochannels, the Al sheet was imprinted using a silicon mold (hexagonally ordered pillar array with height of  $200 \text{ nm}$ , diameter of  $200 \text{ nm}$ , and pitch of  $500 \text{ nm}$ ) with a pressure of  $\approx 2 \times 10^4 \text{ N cm}^{-2}$ . For the semioordered nanochannel growth, the imprinting step was skipped. Then a  $200 \text{ V}$  anodic anodization and subsequent barrier thinning were carried out with the Al chip to get a large pore ( $\sim 200 \text{ nm}$  in diameter) PAM layer with a thin barrier ( $\text{Al}_2\text{O}_3$ ) layer, with the details reported by us before.<sup>21</sup> This layer of large pore PAM thickness was controlled to be  $\sim 1 \mu\text{m}$ . Finally, a  $5 \text{ V}$  anodic anodization was executed continuously on the chip to obtain the underlying small pore PAM layer in  $5 \text{ vol} \% \text{ H}_2\text{SO}_4$  aqueous solution under  $10 \text{ }^\circ\text{C}$ . This layer thickness was controlled by the anodization time, where the growth rate was  $\sim 0.5 \mu\text{m h}^{-1}$ . The chip was rinsed by DI water and dried by compressed air after every step.

**MAPbI<sub>3</sub> Growth in PAMs.** Before the VSSR growth, the Pb precursor was electrochemically deposited in the dual-diameter PAMs. Different from what has been used for Pb deposition in PAMs, a mixture of water and dimethyl sulfoxide (DMSO) (1:1 by vol) was used as the electrolyte for the large amount of Pb deposition to avoid water splitting. Specifically,  $13.905 \text{ g}$  of  $\text{PbCl}_2$  powder was dissolved in  $500 \text{ mL}$  of water–DMSO mixture solvent to get a saturated ( $0.1 \text{ M}$ ) solution, and the solution was stirred under  $80 \text{ }^\circ\text{C}$  conditions overnight. The electrochemical deposition was conducted with a three-electrode system with an alternating current method by using a potentiostat (SG 300, Gamry Instruments). A  $50 \text{ Hz}$  sinusoidal voltage was applied for  $15 \text{ min}$ , and the amplitude was adjusted from  $6$  to  $9 \text{ V}$  to maintain a peak current density of  $2.2 \text{ mA cm}^{-2}$  at the negative deposition cycle. The chip was rinsed by deionized (DI) water and dried by compressed air afterward. The following VSSR growth of the perovskite materials exactly followed the method reported by us before.<sup>21,31</sup>

**MAPbI<sub>3</sub> QW/NW Membrane Delamination.** The membrane delamination from the Al substrate was achieved by a  $\text{HgCl}_2/\text{IPA}$  etching process. Specifically, after MAPbI<sub>3</sub> growth, the chip was mounted onto a glass substrate with the utilization of UV curable epoxy (NOA 81). Then, the chip was put into the  $\text{HgCl}_2/\text{IPA}$  solution with saturated concentration for  $4 \text{ h}$  under room temperature to fully etch away the Al foil. Note that the backside of the chip was gently scratched by a knife to exposure the Al foil before the etch process. After rinsing in IPA several times, the chip was dried by compressed air.

**Device Fabrication.** A mild surface ion milling process was carried out to remove the surface overgrown perovskite thin film before the electrode deposition. Specifically, argon ions were accelerated by  $100 \text{ V}$  voltage in a vacuum of  $1.4 \times 10^{-4} \text{ Torr}$  to bombard the sample surface for  $1 \text{ h}$ . The angle between the ion acceleration path and the normal of the chip is

80° with continuous rotation of the chip during the milling process. The following device fabrication process is schematically shown in Supporting Information Figure S2. First, two ITO strip electrodes (2 cm in length, 1.5 mm in width, and 5 mm in interval) were sputtered on the surface under low RF power (50 W). The base pressure and working pressure for sputtering were  $4 \times 10^{-4}$  Pa and  $2 \times 10^{-1}$  Pa, respectively. After the thin Cu wire bonding on the ITO electrode, the HgCl<sub>2</sub>/IPA etching process was carried out to remove the bottom Al foil. Then, another 150 nm ITO electrode was sputtered onto the chip with the same shadow mask to form the cross-bar device. After the top electrode wire bonding, a thin layer of PMMA was spin coated onto the device for the packaging. For the flexible device fabrication, the glass substrate was changed to a polyethylene terephthalate (PET) substrate. After the final step of wire bonding, the device/epoxy membrane was peeled off from the PET substrate. Note that the adhesion between the epoxy and the PET substrate was not strong. The membrane could be easily peeled off after gently delaminating a corner with a knife. The freestanding device/epoxy membrane was packaged by polydimethylsiloxane (PDMS) to get the final flexible device.

**Characterization.** SEM images were characterized using field-emission scanning electron microscope (JEOL JSM-7100F) that was equipped with a Si (Li) detector and PGT 4000T analyzer for energy dispersive X-ray (EDX) mapping of perovskite NWs embedded in PAMs. Using an accelerating voltage of 10 kV, the elemental mappings were recorded by counting for 100 s. HAADF-STEM images were obtained by a double spherical aberration corrected STEM (FEI Themis Cubed G2) with 300 kV acceleration voltage and 100 pA current. The convergence semiangle was 25 mrad, and the camera length was 115 mm. The cross-sectional TEM specimen was prepared by focused ion beam (FIB, FEI Helios 600i) cutting. The UV-vis absorption spectrum was measured using a Varian Cary 500 spectrometer (Varian, U.S.A.). PL spectra and TRPL curves were obtained with an Edinburgh FSS fluorescence spectrometer equipped with a xenon lamp and a pulsed LED (365 nm). Note that the samples for both the UV-vis absorption and PL/TRPL measurement had no bottom Al foil, where the HgCl<sub>2</sub> etching process mentioned above had been executed. The photodetector device was characterized using a HP 4156A analyzer along with a probe station (Sigatone, U.S.A.) and also a Newport IPCE measurement system.

## ■ ASSOCIATED CONTENT

### SI Supporting Information

The Supporting Information is available free of charge at <https://pubs.acs.org/doi/10.1021/acs.nanolett.2c00383>.

Double-exponential fitting results for MAPbI<sub>3</sub> NW and QW PL decay profiles, MAPbI<sub>3</sub> QW/NW array characterization, device fabrication process flow, absolute EQE spectra, band alignment of the QW/NW array based NPD device, response time characterization of the NPD device, wavelength dependent light intensities, SEM images of grown chips with different QW layer thicknesses, and photograph of a flat membrane (PDF)

## ■ AUTHOR INFORMATION

### Corresponding Author

Zhiyong Fan – Department of Electronic and Computer Engineering, The Hong Kong University of Science and Technology, Kowloon, Hong Kong SAR 000000, China; Guangdong-Hong Kong-Macao Joint Laboratory for Intelligent Micro-Nano Optoelectronic Technology, The Hong Kong University of Science and Technology, Kowloon, Hong Kong SAR 000000, China; [orcid.org/0000-0002-5397-0129](https://orcid.org/0000-0002-5397-0129); Email: [eezfan@ust.hk](mailto:eezfan@ust.hk)

### Authors

Daquan Zhang – Department of Electronic and Computer Engineering, The Hong Kong University of Science and Technology, Kowloon, Hong Kong SAR 000000, China

Yudong Zhu – Department of Electronic and Computer Engineering, The Hong Kong University of Science and Technology, Kowloon, Hong Kong SAR 000000, China; Department of Materials Science and Engineering, Shenzhen Key Laboratory of Full Spectral Solar Electricity Generation (FSSEG), Southern University of Science and Technology, Shenzhen, Guangdong 518055, China

Qianpeng Zhang – Department of Electronic and Computer Engineering, The Hong Kong University of Science and Technology, Kowloon, Hong Kong SAR 000000, China

Beitao Ren – Department of Electronic and Computer Engineering, The Hong Kong University of Science and Technology, Kowloon, Hong Kong SAR 000000, China

Bryan Cao – Department of Electronic and Computer Engineering, The Hong Kong University of Science and Technology, Kowloon, Hong Kong SAR 000000, China

Qizhen Li – School of Materials, University of Manchester, Manchester M139PL, United Kingdom

Swapnadeep Poddar – Department of Electronic and Computer Engineering, The Hong Kong University of Science and Technology, Kowloon, Hong Kong SAR 000000, China

Yu Zhou – Department of Electronic and Computer Engineering, The Hong Kong University of Science and Technology, Kowloon, Hong Kong SAR 000000, China; [orcid.org/0000-0001-7233-4649](https://orcid.org/0000-0001-7233-4649)

Xiao Qiu – Department of Electronic and Computer Engineering, The Hong Kong University of Science and Technology, Kowloon, Hong Kong SAR 000000, China

Zhubing He – Department of Materials Science and Engineering, Shenzhen Key Laboratory of Full Spectral Solar Electricity Generation (FSSEG), Southern University of Science and Technology, Shenzhen, Guangdong 518055, China; [orcid.org/0000-0002-2775-0894](https://orcid.org/0000-0002-2775-0894)

Complete contact information is available at: <https://pubs.acs.org/10.1021/acs.nanolett.2c00383>

### Author Contributions

Z.F. and D.Z. conceived the ideas, and Z.F. supervised the work; D.Z. grew the QW/NW samples and carried out optical spectroscopy, XRD, SEM, and EDX characterizations; Y.Z. did the FIB and TEM characterization with help from Q.L.; D.Z. fabricated and characterized the devices with help from Q.Z., B.R., B.C., S.P., Y.Z., and X.Q.; D.Z. and Z.F. carried out the data analysis; D.Z., Z.F., and Z.H. wrote the manuscript; all authors discussed the results and commented on the manuscript.

## Notes

The authors declare no competing financial interest.

## ACKNOWLEDGMENTS

This work was financially supported by Hong Kong Research Grant Council (General Research Fund Project Nos. 16309018, 16214619, 16205321), Innovation Technology Commission Fund (Project No. GHP/014/19SZ), Shen Zhen Science and Technology Innovation Commission (Project No. JCYJ20170818114107730), Guangdong-Hong Kong-Macao Intelligent Micro-Nano Optoelectronic Technology Joint Laboratory (Grant No. 2020B1212030010), and Foshan Innovative and Entrepreneurial Research Team Program (2018IT100031). The authors also acknowledge the support from the Material Characterization and Preparation Facility (MCPF), the Center for 1D/2D Quantum Materials, and the State Key Laboratory on Advanced Displays and Optoelectronics Technologies at HKUST.

## REFERENCES

- (1) Dou, L.; Yang, Y. M.; You, J.; Hong, Z.; Chang, W. H.; Li, G.; Yang, Y. Solution-processed hybrid perovskite photodetectors with high detectivity. *Nat. Commun.* **2014**, *5* (1), 5404.
- (2) Saidaminov, M. I.; Adinolfi, V.; Comin, R.; Abdelhady, A. L.; Peng, W.; Dursun, I.; Yuan, M.; Hoogland, S.; Sargent, E. H.; Bakr, O. M. Planar-integrated single-crystalline perovskite photodetectors. *Nat. Commun.* **2015**, *6* (1), 8724.
- (3) Wang, H. P.; Li, S.; Liu, X.; Shi, Z.; Fang, X.; He, J. H. Low-Dimensional Metal Halide Perovskite Photodetectors. *Adv. Mater.* **2021**, *33* (7), No. 2003309.
- (4) Ahmadi, M.; Wu, T.; Hu, B. A Review on Organic-Inorganic Halide Perovskite Photodetectors: Device Engineering and Fundamental Physics. *Adv. Mater.* **2017**, *29* (41), 1605242.
- (5) Dong, Y. H.; Zou, Y. S.; Song, J. Z.; Song, X. F.; Zeng, H. B. Recent progress of metal halide perovskite photodetectors. *Journal of Materials Chemistry C* **2017**, *5* (44), 11369–11394.
- (6) Li, L.; Ye, S.; Qu, J.; Zhou, F.; Song, J.; Shen, G. Recent Advances in Perovskite Photodetectors for Image Sensing. *Small* **2021**, *17* (18), No. 2005606.
- (7) Chen, Q.; Wu, J.; Ou, X.; Huang, B.; Almutlaq, J.; Zhumekenov, A. A.; Guan, X.; Han, S.; Liang, L.; Yi, Z.; Li, J.; Xie, X.; Wang, Y.; Li, Y.; Fan, D.; Teh, D. B. L.; All, A. H.; Mohammed, O. F.; Bakr, O. M.; Wu, T.; Bettinelli, M.; Yang, H.; Huang, W.; Liu, X. All-inorganic perovskite nanocrystal scintillators. *Nature* **2018**, *561* (7721), 88–93.
- (8) Bao, C.; Yang, J.; Bai, S.; Xu, W.; Yan, Z.; Xu, Q.; Liu, J.; Zhang, W.; Gao, F. High Performance and Stable All-Inorganic Metal Halide Perovskite-Based Photodetectors for Optical Communication Applications. *Adv. Mater.* **2018**, *30* (38), No. 1803422.
- (9) Hu, W.; Huang, W.; Yang, S.; Wang, X.; Jiang, Z.; Zhu, X.; Zhou, H.; Liu, H.; Zhang, Q.; Zhuang, X.; et al. High-Performance Flexible Photodetectors based on High-Quality Perovskite Thin Films by a Vapor–Solution Method. *Adv. Mater.* **2017**, *29* (43), 1703256.
- (10) Hao, D.; Zou, J.; Huang, J. Recent developments in flexible photodetectors based on metal halide perovskite. *InfoMat* **2020**, *2* (1), 139–169.
- (11) Fang, Y. J.; Dong, Q. F.; Shao, Y. C.; Yuan, Y. B.; Huang, J. S. Highly narrowband perovskite single-crystal photodetectors enabled by surface-charge recombination. *Nat. Photonics* **2015**, *9* (10), 679.
- (12) Lin, Q. Q.; Armin, A.; Burn, P. L.; Meredith, P. Filterless narrowband visible photodetectors. *Nat. Photonics* **2015**, *9* (10), 687.
- (13) Saidaminov, M. I.; Haque, M. A.; Savoie, M.; Abdelhady, A. L.; Cho, N.; Dursun, I.; Buttner, U.; Alarousu, E.; Wu, T.; Bakr, O. M. Perovskite Photodetectors Operating in Both Narrowband and Broadband Regimes. *Adv. Mater.* **2016**, *28* (37), 8144–8149.
- (14) Li, J.; Wang, J.; Ma, J.; Shen, H.; Li, L.; Duan, X.; Li, D. Self-trapped state enabled filterless narrowband photodetections in 2D layered perovskite single crystals. *Nat. Commun.* **2019**, *10* (1), 806.
- (15) Wang, J.; Xiao, S.; Qian, W.; Zhang, K.; Yu, J.; Xu, X.; Wang, G.; Zheng, S.; Yang, S. Self-Driven Perovskite Narrowband Photodetectors with Tunable Spectral Responses. *Adv. Mater.* **2021**, *33* (3), No. 2005557.
- (16) Wang, J.; Xu, X. W.; Xiao, S.; Li, Y.; Qian, W.; Yu, J.; Zhang, K.; Yang, S. H. Self-Driven Perovskite Dual-Band Photodetectors Enabled by a Charge Separation Reversion Mechanism. *Advanced Optical Materials* **2021**, *9* (17), 2100517.
- (17) Lukac, R. Single-sensor imaging in consumer digital cameras: a survey of recent advances and future directions. *Journal of Real-Time Image Processing* **2006**, *1* (1), 45–52.
- (18) Nishiwaki, S.; Nakamura, T.; Hiramoto, M.; Fujii, T.; Suzuki, M. Efficient colour splitters for high-pixel-density image sensors. *Nat. Photonics* **2013**, *7* (3), 240–246.
- (19) Lyons, D. M.; Armin, A.; Stolterfoht, M.; Nagiri, R. C. R.; Jansen-van Vuuren, R. D.; Pal, B. N.; Burn, P. L.; Lo, S. C.; Meredith, P. Narrow band green organic photodiodes for imaging. *Org. Electron.* **2014**, *15* (11), 2903–2911.
- (20) Sobhani, A.; Knight, M. W.; Wang, Y.; Zheng, B.; King, N. S.; Brown, L. V.; Fang, Z.; Nordlander, P.; Halas, N. J. Narrowband photodetection in the near-infrared with a plasmon-induced hot electron device. *Nat. Commun.* **2013**, *4* (1), 1643.
- (21) Gu, L.; Tavakoli, M. M.; Zhang, D.; Zhang, Q.; Waleed, A.; Xiao, Y.; Tsui, K. H.; Lin, Y.; Liao, L.; Wang, J.; Fan, Z. 3D Arrays of 1024-Pixel Image Sensors based on Lead Halide Perovskite Nanowires. *Adv. Mater.* **2016**, *28* (44), 9713–9721.
- (22) Gu, L.; Poddar, S.; Lin, Y.; Long, Z.; Zhang, D.; Zhang, Q.; Shu, L.; Qiu, X.; Kam, M.; Javey, A.; Fan, Z. A biomimetic eye with a hemispherical perovskite nanowire array retina. *Nature* **2020**, *581* (7808), 278–282.
- (23) Shoaib, M.; Zhang, X.; Wang, X.; Zhou, H.; Xu, T.; Wang, X.; Hu, X.; Liu, H.; Fan, X.; Zheng, W.; Yang, T.; Yang, S.; Zhang, Q.; Zhu, X.; Sun, L.; Pan, A. Directional Growth of Ultralong CsPbBr<sub>3</sub> Perovskite Nanowires for High-Performance Photodetectors. *J. Am. Chem. Soc.* **2017**, *139* (44), 15592–15595.
- (24) Feng, J. G.; Gong, C.; Gao, H. F.; Wen, W.; Gong, Y. J.; Jiang, X. Y.; Zhang, B.; Wu, Y. C.; Wu, Y. S.; Fu, H. B.; Jiang, L.; Zhang, X. Single-crystalline layered metal-halide perovskite nanowires for ultrasensitive photodetectors. *Nature Electronics* **2018**, *1* (7), 404–410.
- (25) Waleed, A.; Tavakoli, M. M.; Gu, L. L.; Hussain, S.; Zhang, D. Q.; Poddar, S.; Wang, Z. Y.; Zhang, R. J.; Fan, Z. Y. All Inorganic Cesium Lead Iodide Perovskite Nanowires with Stabilized Cubic Phase at Room Temperature and Nanowire Array-Based Photodetectors. *Nano Lett.* **2017**, *17* (8), 4951–4957.
- (26) Waleed, A.; Tavakoli, M. M.; Gu, L.; Wang, Z.; Zhang, D.; Manikandan, A.; Zhang, Q.; Zhang, R.; Chueh, Y. L.; Fan, Z. Lead-Free Perovskite Nanowire Array Photodetectors with Drastically Improved Stability in Nanoengineering Templates. *Nano Lett.* **2017**, *17* (1), 523–530.
- (27) Gu, L. L.; Zhang, D. Q.; Kam, M.; Zhang, Q. P.; Poddar, S.; Fu, Y.; Mo, X. L.; Fan, Z. Y. Significantly improved black phase stability of FAPbI<sub>3</sub> nanowires via spatially confined vapor phase growth in nanoporous templates. *Nanoscale* **2018**, *10* (32), 15164–15172.
- (28) Deng, W.; Huang, L.; Xu, X.; Zhang, X.; Jin, X.; Lee, S. T.; Jie, J. Ultrahigh-Responsivity Photodetectors from Perovskite Nanowire Arrays for Sequentially Tunable Spectral Measurement. *Nano Lett.* **2017**, *17* (4), 2482–2489.
- (29) Yang, T.; Zheng, Y.; Du, Z.; Liu, W.; Yang, Z.; Gao, F.; Wang, L.; Chou, K.-C.; Hou, X.; Yang, W. Superior photodetectors based on all-inorganic perovskite CsPbI<sub>3</sub> nanorods with ultrafast response and high stability. *ACS Nano* **2018**, *12* (2), 1611–1617.
- (30) Lin, C. H.; Kang, C. Y.; Wu, T. Z.; Tsai, C. L.; Sher, C. W.; Guan, X.; Lee, P. T.; Wu, T.; Ho, C. H.; Kuo, H. C.; et al. Giant optical anisotropy of perovskite nanowire array films. *Adv. Funct. Mater.* **2020**, *30* (14), 1909275.
- (31) Zhang, D.; Gu, L.; Zhang, Q.; Lin, Y.; Lien, D. H.; Kam, M.; Poddar, S.; Garnett, E. C.; Javey, A.; Fan, Z. Increasing Photoluminescence Quantum Yield by Nanophotonic Design of Quantum



Confined Halide Perovskite Nanowire Arrays. *Nano Lett.* **2019**, *19* (5), 2850–2857.

(32) Gu, L.; Tavakoli, M. M.; Zhang, D.; Zhang, Q.; Waleed, A.; Xiao, Y.; Tsui, K. H.; Lin, Y.; Liao, L.; Wang, J.; et al. 3D Arrays of 1024-pixel image sensors based on lead halide perovskite nanowires. *Adv. Mater.* **2016**, *28* (44), 9713–9721.

(33) Zhang, Q.; Zhang, D.; Gu, L.; Tsui, K.-H.; Poddar, S.; Fu, Y.; Shu, L.; Fan, Z. Three-dimensional perovskite nanophotonic wire array-based light-emitting diodes with significantly improved efficiency and stability. *ACS Nano* **2020**, *14* (2), 1577–1585.

(34) Zhang, D.; Zhang, Q.; Ren, B.; Zhu, Y.; Abdellah, M.; Fu, Y.; Cao, B.; Wang, C.; Gu, L.; Ding, Y.; Tsui, K.-H.; Fan, S.; Poddar, S.; Shu, L.; Zhang, Y.; Kuang, D.-B.; Liao, J.-F.; Lu, Y.; Zheng, K.; He, Z.; Fan, Z. Large-scale planar and spherical light-emitting diodes based on arrays of perovskite quantum wires. *Nat. Photonics* **2022**, in press DOI: 10.1038/s41566-022-00978-0.

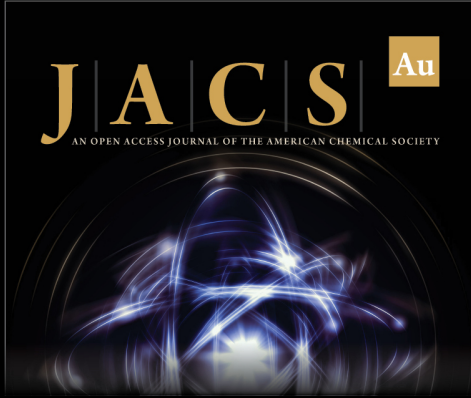
(35) Kwon, K. C.; Hong, K.; Van Le, Q.; Lee, S. Y.; Choi, J.; Kim, K. B.; Kim, S. Y.; Jang, H. W. Inhibition of ion migration for reliable operation of organolead halide perovskite-based Metal/Semiconductor/Metal broadband photodetectors. *Adv. Funct. Mater.* **2016**, *26* (23), 4213–4222.

(36) Zou, H.; Dai, G.; Wang, A. C.; Li, X.; Zhang, S. L.; Ding, W.; Zhang, L.; Zhang, Y.; Wang, Z. L. Alternating current photovoltaic effect. *Adv. Mater.* **2020**, *32* (11), 1907249.


(37) Chen, S.; Li, S.; Peng, S.; Huang, Y.; Zhao, J.; Tang, W.; Guo, X. Silver nanowire/polymer composite soft conductive film fabricated by large-area compatible coating for flexible pressure sensor array. *Journal of Semiconductors* **2018**, *39* (1), 013001.


(38) Cheng, T.; Wu, Y.; Shen, X.; Lai, W.; Huang, W. Inkjet printed large-area flexible circuits: a simple methodology for optimizing the printing quality. *Journal of Semiconductors* **2018**, *39* (1), 015001.


(39) Wang, D.; Mei, Y.; Huang, G. Printable inorganic nanomaterials for flexible transparent electrodes: from synthesis to application. *Journal of Semiconductors* **2018**, *39* (1), 011002.



**JACS** Au  
AN OPEN ACCESS JOURNAL OF THE AMERICAN CHEMICAL SOCIETY

 Editor-in-Chief  
**Prof. Christopher W. Jones**  
Georgia Institute of Technology, USA

**Open for Submissions** 

pubs.acs.org/jacsau  ACS Publications  
Most Trusted. Most Cited. Most Read.